Geophys. J. Int. (2006) **164,** 218–235 doi: 10.1111/j.1365-246X.2005.02791.x

Moho depth and three-dimensional *P* and *S* structure of the crust and uppermost mantle in the Eastern Mediterranean and Middle East derived from tomographic inversion of local ISC data

Ivan Koulakov[1,2]* and Stephan V. Sobolev[1]

[1] *GeoForschungsZentrum-Potsdam, Telegrafenberg,* 14473*, Potsdam, Germany. E-mail: ivan@gfz-potsdam.de*
[2] *Institute of Geology SB RAS, Prosp. Akademika Koptyuga,* 3*,* 630090*, Novosibirsk, Russia. E-mail: kul@uiggm.nsc.ru*

Accepted 2005 August 16. Received 2005 June 20; in original form 2004 August 9

SUMMARY

∼82 000 *P* and *S* arrival times from ∼3000 sources recorded by ∼250 seismic stations from the revised ISC catalogue are employed to study a circular area of 6° radius centred on the Dead Sea. We use the linearized tomographic approach based on the rays constructed in a 1-D spherical velocity model and corrected for the Moho depth variation and relief. All the sources were relocated. As the result of simultaneous iterative inversion we get 3-D *P* and *S* velocity anomalies in the crust and uppermost mantle, Moho depth and corrected source parameters. The resulting images fit well with the existing tectonic elements in the study area. In the crust, a narrow *P* and *S* low-velocity anomaly marks the position of the Dead Sea Transform (DST) that is interpreted as sediments in the shallower layer and a zone of fractured and deformed rocks in the middle and lower crust. There is a narrow (50 km wide) band of thickening of the crust along the DST in the Arava valley between the Red Sea and Dead Sea and some 100 km north of the Dead Sea. This zone may be associated with the minimum of the lithospheric strength and, therefore, explain the location of the DST in the Arava Valley. The velocity anomalies under the crust and the map of the Moho depth clearly distinguish the oceanic (Levant basin) and continental types of crust (Asia Minor, Zagros, Cyprus and Eratosthenes Mount). Verification of the results takes an important part in this study. Inversions of different starting models and independent processing of data subsets show high robustness of the results. Synthetic tests clearly show the limits of the resolving power of the inversion with the existing data set.

Key words: crustal structure, Eastern Mediterranean, local tomography, Middle East, Moho depth.

1 INTRODUCTION

The study area (Fig. 1) comprises a zone of transition from the intermediate semi-oceanic crust in the Mediterranean region to the continental crust of the Arabian shield in the east and the Taurus Mountains in the north. The eastern Mediterranean studied in this work can be subdivided into several blocks. The eastern part is occupied by the Levant basin, up to 2.2 km deep. On its western side lies the Eratosthenes Seamount, the top of which rises to about 0.8 km below sea level. In the northern part of the basin, near Cyprus, a complex system apparently related to a recent subduction zone is observed.

The Eastern Mediterranean evolved through a long and complex geological history, which started in the Late Triassic–Early Jurassic time (e.g. Garfunkel 1998). As a result, the crust is composed of a variety of different units. Crustal variability is one of the most important factors controlling the tectonic evolution of this region. The formation of the Levant basin was associated with the evolution of the Neo-Tethys Ocean and its margins. Its history was closely related to the Alpine orogen. The nature of the Eastern Mediterranean has been the subject of numerous studies over a long time. There is considerable agreement on the broad picture, but many problems remain unsolved. A series of different geophysical studies, such as refraction–reflection profiles (Makris *et al.* 1983; Ben-Avraham *et al.* 2002), gravity (Rybakov *et al.* 2000; Seber *et al.* 2001), receiver function (Sandvol *et al.* 1998; Hofstetter & Bock 2004; Mohsen *et al.* 2005), complex seismic, gravity and magnetic studies (Ginzburg & Ben-Avraham 1992) have provided rich information about the crustal structure in the Eastern Mediterranean. However, in spite of numerous geophysical works in this region, there is no agreement on the nature of the crust or its age.

The eastern part of the study area includes the continental region along the eastern Mediterranean coast. The most striking feature of this region is the Dead Sea transform (DST), a plate boundary which separates the Arabian plate from the African plate. This is a

* Now at: GFZ Potsdam, Telegrafenberg, 14473, Potsdam, Germany (*until August 2006*).

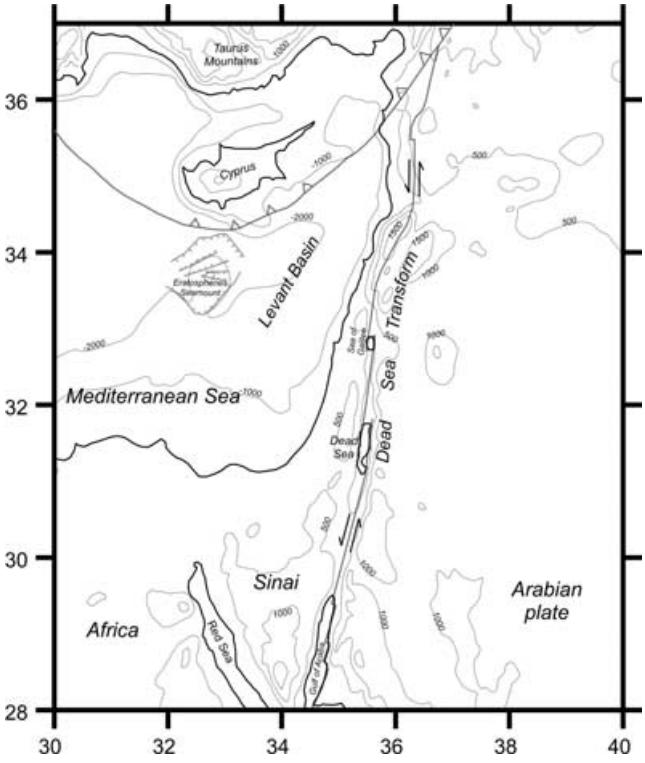

Figure 1. Study area: relief, bathymetry and some tectonic elements.

dominant tectonic element of this area and its formation controls the present-day tectonic pattern in Asia Minor. Motions along the DST probably started during the Early to Middle Miocene. Since that time, 105 km of left lateral horizontal displacement has occurred along its length (Freund *et al.* 1970).

Until recently, the western and eastern flanks of the DST were studied independently. The western part of the DST was investigated with the use of a variety of different geophysical methods: gravity (ten Brink *et al.* 1993), active seismics (Ginzburg *et al.* 1979; Ginzburg & Ben-Avraham 1997), teleseismic tomography (Hofstetter *et al.* 1991, 2000), receiver function (Hofstetter & Bock 2004) and others. The eastern part of the transform was studied by El-Isa *et al.* (1987), Kovach *et al.* (1990), Al-Zoubi & Ben-Avraham (2002) and others. Only during the last years, integrated studies on both flanks of the DST were realized thanks to the international DESERT project, resulting in a detailed complex geophysical investigation across the DST (DESERT Group 2004). One of the important results of this project is the topography of the Moho interface across the DST. Different geophysical studies, such as near vertical seismic reflections and wide-angle seismic refractions/reflections, receiver function analysis and gravity modelling provide consistent values of the Moho depth. According to these studies, the crustal thickness increases gradually from 26 km under the Mediterranean coast to 39 km under the Jordan highlands.

The earlier observations of the crustal thickness in the area published by Ziegler (1990), Blundell *et al.* (1992), Meissner *et al.* (1987), Seber *et al.* (1997), Beloussov *et al.* (1991) and Li & Mooney (1998) have been summarized in $1^\circ \times 1^\circ$ crustal model (http://mahi.ucsd.edu/Gabi/sediment.html, Laske, private communication, 2004). For the study area, this model suggests a rather smooth Moho transition from oceanic crust in the Eastern Mediterranean (24 km depth, minimum) to continental crust in the Taurus Mountains (40 km) and Asia Minor (37 km).

The regional seismic structure of the crust and upper mantle in the Eastern Mediterranean and Asia Minor was studied in some tomographic works at regional and global scales (Spakman 1991; Bijwaard *et al.* 1998; Martinez *et al.* 2000; Pasyanos & William 2002; Piromallo & Morelli 2003). In general, all these models agree that the transition from the Mediterranean to the continental crust in Asia Minor coincides with the velocity contrast from fast velocities under the sea to low velocities in the continental crust.

Despite the large number of geophysical studies, it is still problematic to construct a high-resolution crustal model for the whole region. Few wide-angle reflection/refraction lines do not allow for robust detailed interpolation. The crustal maps derived from the gravity field suffer from intrinsic ambiguity and the global models based on seismic data have too low resolution. The main purpose of this study is to create a regional map of the Moho depth and 3-D velocity model of the crust and the uppermost mantle in the Eastern Mediterranean that are more detailed than the existing global and regional models. To achieve maximum robustness of the models we use very conservative criteria in data selection and perform numerous different resolution tests.

2 DATA

In this study, we use the traveltimes reported by the International Seismological Center (ISC 2001). The ISC catalogue is an enormous data bank, which provides rich information for exploration of the Earth at different scales. The undoubted advantage of the ISC data is their continuance over several decades and their global coverage. No local network can provide such a long duration of observations. At the same time, the locations of the sources provided by the ISC need to be revised. In this study, the ISC source coordinates were only used for initial selection of data. The algorithm only takes the arrival times of the rays as the input. The data processing starts with the absolute location of the sources.

The information from the ISC catalogue used in this study has no uniform density within the study region (Fig. 2). The best data

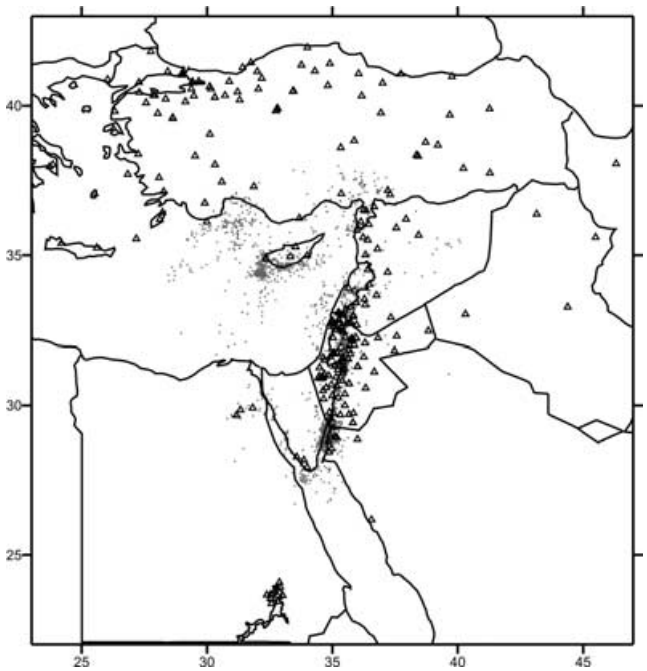

Figure 2. Distribution of local and regional seismic stations (triangles) and events (grey dots) from the ISC catalogue.

coverage is in the Asia Minor to the south of the Dead Sea basin and along the DST. The rather large number of permanent stations in the region and their dense distribution allow a good determination of local earthquakes parameters. Another big cluster of earthquakes is situated to the south of Cyprus where subduction is taking place (e.g. Garfunkel 1998). However, these events are mostly localized using the remote stations in Turkey and Asia Minor, and the location accuracy there is worse than in Asia Minor. In the other parts of the study region, the density of the initial information is significantly lower.

This study is based on arrival times of crustal rays (*Pg*, *Sg*, *Pn*, *Sn*) from the ISC catalogues in the time period from 1964 to 2001 (ISC 2001). About 3000 events in a circle of 6° radius centred on the Dead Sea basin were selected. In total, about 82 000 *P* and *S* rays with epicentral distances limited to 6° were employed. According to this selection criterion, about 250 seismic stations in the surrounding areas contributed data for this work. For each event we required no less than 25 records and a GAP of no more than 180°. These quite strict requirements ensure significant improvement of source location accuracy.

3 ALGORITHMS

In this study we perform an iterative simultaneous inversion for source parameters, *P* and *S* velocity model and Moho depth. Today there is a lot of different seismic tomography algorithms for different scales of problems. On the local scale, one of the most popular methods of simultaneous determination of source parameters and velocity model is the SIMULP code developed by Evans *et al.* (1994). However, our algorithm has some important features compared to with this and other codes:

(i) We invert for *P* and *S* velocity. We find the way of inversion for *P* and *P*/*S* parameters performed in many studies (e.g. Thurber 1993; Evans *et al.* 1994) not positive, since it does not allow comparison of *P* and *S* models, the similarity of which is one of the most important verification factors.

(ii) We perform the inversion in a much larger area than that allowed by SIMULP and other local tomography codes.

(iii) Our algorithm allows investigation of the Moho depth variation.

(iv) We pay special attention to rejection of outliers and phase re-identification at the step of preliminary source location.

3.1 Reference model and traveltimes

The basic reference model has a 1-D spherical distribution (Model 1, Table 1). In the crust we fix a constant velocity gradient derived from averaging of the crustal velocities obtained by DESERT Group (2004). At the same time, as will be shown in the section on verification (Section 5.2), the reference velocities in the crust do not have a significant effect upon the resulting velocity anomalies. In the uppermost mantle the velocities are taken from the AK135 Model (Kennett *et al.* 1995). In the initial stage, a table of traveltimes of *P* and *S* body waves in a 1-D velocity model for different depths of the sources was computed. This time table allows fast determination of the parameters of the main rays between a source at some depth and a station located at the sea level at some epicentral distance from the source.

However, utilization of a 1-D-reference model for traveltime calculation in areas with strong variation of the Moho depth and surface relief causes significant errors in source location. Within the region studied in this work, the crustal thickness can vary by up to more than 10 km. This corresponds to additional traveltime of up to 1 s. If this factor is not taken into account in the location algorithm, the error of the source location can be up to several tens of kilometres. That is why it is advisable to include into the reference model any information, though rough, about the Moho depth. If there is no information about the regional Moho depth distribution, a global model of crustal thickness (such as the 5° resolution model of Mooney *et al.* 1998) can be used.

In this study, the starting model of the crust is defined on the basis of a 1° × 1° map (Laske, private communication, 2004). The starting model of the Moho depth is shown in Fig. 3.

Non-spherical terms related to the variable Moho depth and surface relief are added to traveltimes, which are computed from the reference table corresponding to each source–receiver couple. If a source is located under the Moho, the correction is computed as follows:

$$dt^{\text{moho}} = dh\ \left[\sqrt{\sigma_1^2 - p^2} - \sqrt{\sigma_2^2 - p^2}\right], \tag{1}$$

where σ_1 and σ_2 are the values of slowness under and above the Moho interface, p is the ray parameter (horizontal component of the slowness vector) and dh is a relative Moho depth at the entry point with respect to the average crustal thickness in the reference model.

For the head rays (travelling below the Moho), the correction for the Moho depth variation is computed with the formula:

$$dt^{\text{moho}} = (dh_1 + dh_2)\sqrt{\sigma_1^2 - \sigma_2^2}, \tag{2}$$

where dh_1 and dh_2 are the crustal variations at the entry and exit points under the source and receiver respectively.

Correction for the topography is computed as:

$$dt^{\text{topo}} = dh\ \sqrt{\sigma^2 - p^2}, \tag{3}$$

where σ is slowness in the uppermost layer and dh is the altitude of the station with respect to sea level.

3.2 Source location algorithm

In this work, the source location is performed in several steps. The first step is an absolute location in a 1-D velocity model corrected

Table 1. Three variants of starting models used to explore robustness of the results.

	Model 1 (main)		Model 2		Model 3	
Moho:	Model 1° × 1° resolution		Flat Moho, 30 km depth		Model 1° × 1° resolution	
Depth, km	*Vp*, km s^{-1}	*Vs*, km s^{-1}	*Vp*, km s^{-1}	*Vs*, km s^{-1}	*Vp*, km s^{-1}	*Vs*, km s^{-1}
0	5.8	3.3	5.8	3.3	6.0	3.4
30	6.7	3.7	6.7	3.7	6.6	3.8
33	7.8	4.45	7.8	4.45	7.8	4.45
77	8.04	4.5	8.04	4.5	8.04	4.5
120	8.05	4.5	8.05	4.5	8.05	4.5

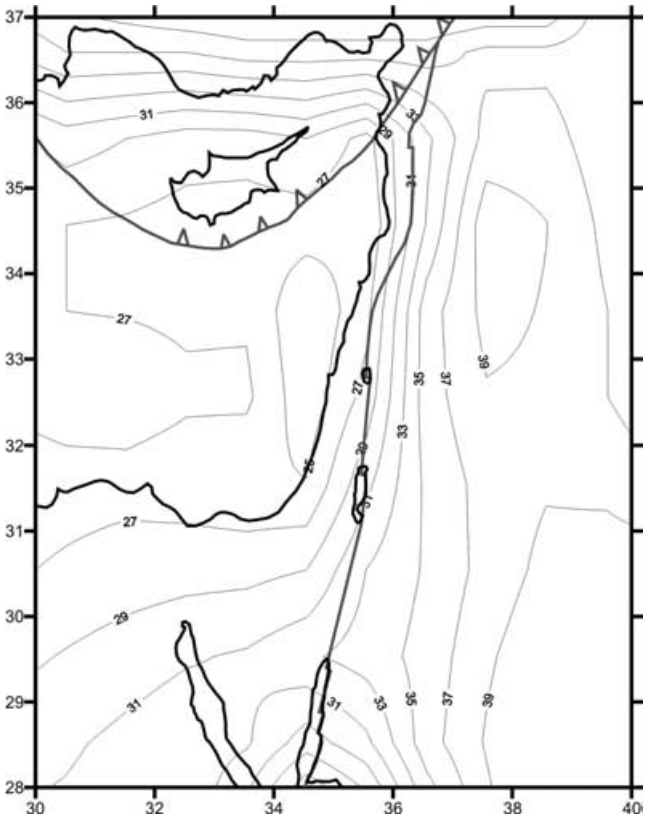

Figure 3. Moho depth in the model CRUST2.0 (Bassin *et al.* 2000, Laske, private communication, 2004) updated with the model with $1^\circ \times 1^\circ$ resolution (Laske, private communication, 2004). This model is taken as a reference in the tomographic inversion.

for the variable Moho depth and topography. The second step is a relative relocation of the sources with the use of the double difference method. The third relocation is performed simultaneously with the determination of velocity anomalies and Moho depth during tomographic inversion. However, the absolute location is a key point of the whole inversion procedure. If the initial position of a source is far away from the real position, further corrections hardly result in the correct solution for the source parameters and velocity anomalies.

One of the main causes of the source location errors is due to outliers in the initial data set. From our estimates, 5–10 per cent of the ISC data have residuals which cannot be explained by a reasonable velocity model. The excessive residuals might be related to wrong picking of phases, operators' mistakes and other subjective and objective factors. They should be rejected from the data set; otherwise a shift of a source from its real position can be up to several tens of kilometres. An additional problem is related to the unknown value of the origin time. Rejection of only one outlier might immediately cause bias of the estimated origin time and change other residuals.

Another source of error is the incorrect identification of phases. For example, if the observed traveltime is between *Pn* and *Pg* reference times, it can be attributed to one or another phase. In the case of wrong phase determination, the value of the residual might have the opposite sign. This would obviously make an impact on the inverted velocities and location parameters.

If the real velocity model is strongly heterogeneous and far from the initial 1-D distribution, the absolute location in the 1-D model would provide a wrong source position. In this case, the shift of the sources from the real position can be so large that the posteriori inversion procedure would not give the true solution.

The algorithm of absolute source location must avoid or reduce these problems. The goal function, which reflects numerically the probability of source position in 4-D space (coordinates and origin time) plays a key role in the location algorithm. We propose a special form of the goal function which can be written as a composition of three terms:

$$G = \sum_{i=1}^{N} A(\Delta t_i) B(d_i) / C_{PS}, \tag{4}$$

where

$$A(\Delta t_i) = \begin{cases} 1, & \text{if } |\Delta t_i| / C_{PS} < \tau_1 \\ (\Delta t_i - \tau_2)/(\tau_1 - \tau_2), & \text{if } \tau_1 < |\Delta t_i| / C_{PS} < \tau_2, \\ 0, & \text{if } |\Delta t_i| / C_{PS} > \tau_2 \end{cases} \tag{5}$$

$$B(d_i) = \begin{cases} 1/d_{\min}, & \text{if } d_i < d_{\min} \\ 1/d_i, & \text{if } d_i > d_{\min} \end{cases}, \tag{6}$$

$$C_{PS} = \begin{cases} 1, & \text{if } P\text{-wave} \\ 1.7, & \text{if } S\text{-wave} \end{cases}, \tag{7}$$

where N is the total number of records of the event, A is a term which reflects the values of residuals, and τ_1 and τ_2 are predefined limits for the values of residuals. If the residual is greater than τ_2, it is considered as an outlier and is not taken into consideration. If a residual is between τ_1 and τ_2, it can be related to velocity anomalies. It might be useful for the tomographic inversion, but in the location procedure its weight should be smaller. Values of τ_1 and τ_2 are determined from expected values of velocity anomalies.

B is a term of the distance dependence. Long rays accumulate more time anomalies along their path and consequently usually have greater residuals. That is why in the location algorithm they should have smaller weight than short rays. $d_{\min}$ is the size of a near zone, where weights of all rays are equal.

C is a term discriminating the phases. Residuals of P rays have greater weight since they are less influenced by velocity perturbations than S rays. At the same time, S residuals are allowed to be greater than P residuals.

The time residuals for the location procedure are computed as:

$$\Delta t_i = t^P_{\text{obs}} - t^P_{\text{ref}} - \Delta t_0 \text{ for } P \text{ waves} \tag{8}$$

$$\Delta t_i = \left(t^S_{\text{obs}} - t^S_{\text{ref}}\right) - \left(t^P_{\text{obs}} - t^P_{\text{ref}}\right) \text{ for } S \text{ waves.} \tag{9}$$

Correction of the origin time Δt_0 is obtained from the condition:

$$\sum_{i=1}^{N_p} B(d_i) \left(t^P_{\text{obs}} - t^P_{\text{ref}} - \Delta t_0\right) = 0, \tag{10}$$

where t^P_{obs} is observed traveltime, t^P_{ref} is a reference traveltime computed with the use of the reference table and corrected for the Moho depth and topography.

Moreover, each individual observation should satisfy the following condition:

$$\left|t^P_{\text{obs}} - t^P_{\text{ref}} - \Delta t_0\right| < \tau_2. \tag{11}$$

All other observations are considered as outliers and are not used in the inversion.

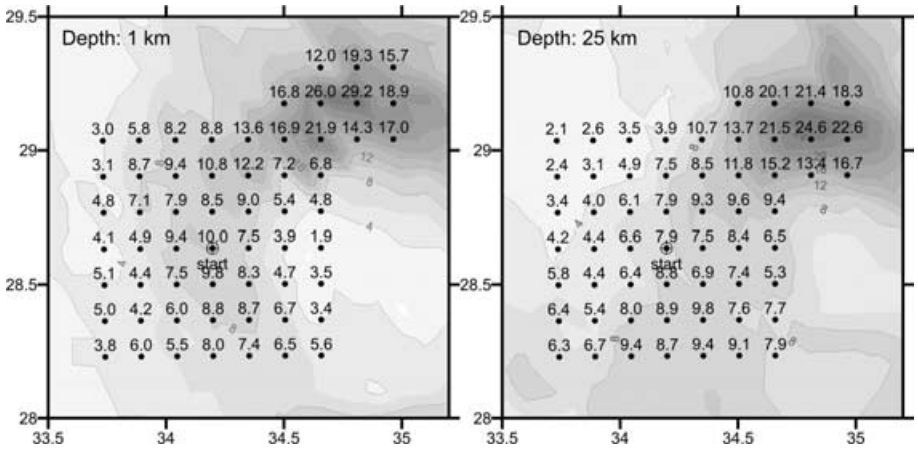

Figure 4. Example of the goal function computed at two depth levels (contour lines). Dots show positions of nodes where the goal function was computed in the location procedure, numbers indicate values of the goal function.

Fig. 4 shows an example of the goal function G for a real earthquake. Here two plots computed at two different depths are presented. The most probable location of the source at each depth is attributed to the point where the goal function is a maximum.

Different approaches can be proposed to solve the problem of determination of the goal function extreme. For example, a gradient descending method allows rather fast convergence. With this method, however, there is a risk that a local maximum is found instead of the true maximum. That is why, in practice, we use a longer but more trustworthy approach. First of all, the goal function is computed on a rather sparse grid at some defined depth levels (three or four), as is shown in Fig. 4. From the level and from the node where the goal function is a maximum, we move up and down searching for a depth where the goal function is maximal. An example of depth dependency for the goal function for a real source is shown in Fig. 5. From the depth where the maximum of the goal function is achieved, further location is performed with the use of a finer grid. As a result, the most probable position of a source in a defined velocity model is attributed to the point where the goal function reaches the maximum value.

3.3 Adjustment of the source position with the double-difference algorithm

The relative position of sources is adjusted with the use of the double-difference method described by Waldhauser & Ellsworth (2000). The main idea is based on an assumption that the residuals from two sources located close to one another recorded at one station should have similar values. The algorithm finds the coordinates and origin time corrections to minimize all possible double differences. The linear equations for all combinations of source couples (for example, with numbers k and m) separated by a distance less than a predefined value $dS^{\max}$ and having a common observation i (the same station and P- or S- phase) are composed:

$$(P_x)_{ik}dx_k + (P_y)_{ik}dy_k + (P_z)_{ik}dz_k + dt^0_k - (P_x)_{im}dx_m - (P_y)_{im}dy_m - (P_z)_{im}dz_m - dt^0_m = dt^{\text{obs}}_{ik} - dt^{\text{obs}}_{im}, \quad (12)$$

where P_x, P_y, P_z are the components of the slowness vector of the corresponding ray at the source point. As a result, there is a system of linear equations with the number of columns equal to the number of sources multiplied by four. Every row contains eight non-zero elements. For 2000 sources, the number of equations is about 1 000 000. This system can be inverted with the use of the iterative LSQR method (van der Sluis & van der Vorst 1987). After inversion, the source parameters are updated and the procedure is repeated again. In total four to five iterations were made.

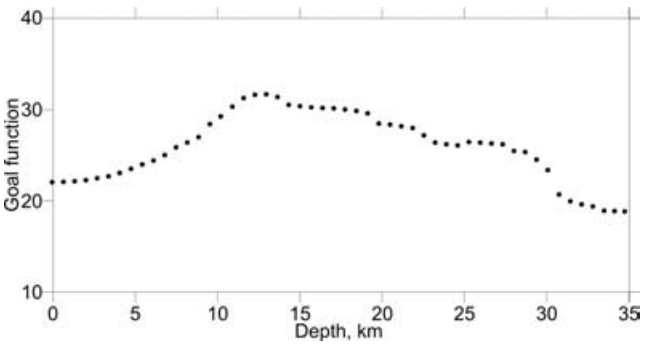

Figure 5. Example of the goal function versus the depth of a source.

3.4 Tomographic inversion

3.4.1 Parametrization

Parametrization of the velocity fields and Moho variation is performed on the basis of the node parametrization method developed in previous works (e.g. Koulakov 1998; Koulakov *et al.* 2002). A certain number of nodes are distributed inside the study volume according to the density of input information. For the 3-D velocity distribution in the crust, the nodes were distributed at some depth levels (at 5, 20, 30, 33 and 60 km). For each level, a function of the ray density was computed as is shown in Figs 6(a)–(c). The nodes were distributed in each level in some parallel lines so that the distance between nodes was inversely proportional to the ray density. To avoid an excessive concentration of nodes, we fix the minimum distance between nodes at 15 km. The nodes for the Moho depth variation are constructed according to the density of the entry and exit points of *Pn* and *Sn* rays at the Moho (Fig. 6d).

A parametrization grid, constructed using this method, has some orientation of lines where the nodes are distributed that can influence the resulting model. To avoid this problem we conduct four separate inversions using four differently orientated grids at 0°, 45°, 90° and 135°, which thus neutralizes most of the artefacts related to grid orientation.

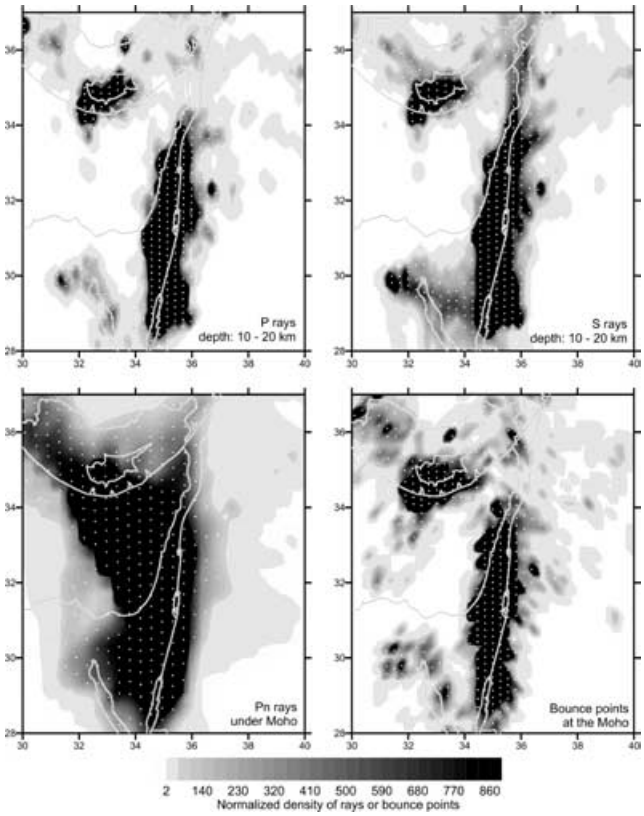

Figure 6. Example of the parametrization grid construction according to the input information density. White dots indicate nodes of a grid. (a) Shows density of *Pg* and *Pn* rays in the depth interval 10–20 km. (b) Similar to plot a, but for the *Sg* and *Sn* rays. (c) Depicts the density of *Pn* rays under the Moho. (d) Is density of bounce points at the Moho. Contour lines show normalized density of rays or bounce points according to the scale.

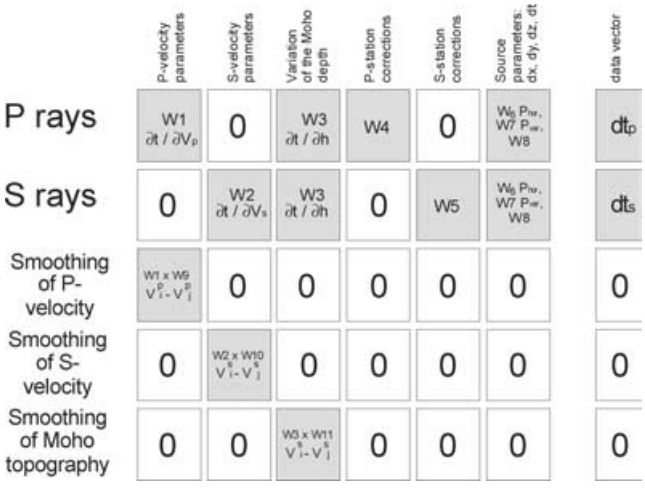

Figure 7. General structure of the matrix for inversion of different parameters.

3.4.2 Matrix construction and inversion

The general structure of the matrix is shown in Fig. 7. The vertical columns of the matrix contain the information for the following groups of parameters: 3-D *P* and *S* velocity models (M^{Vgp}, M^{Vgs}); 2-D variations of the Moho depth (M^{dh}); parameters for the source relocation (four parameters for each source) (M^{srce}); *P* and *S* station corrections (M^{Stp}, M^{Sts}).

The matrix elements responsible for the *P* and *S* velocity fields are computed on the basis of the rays traced after the double-difference algorithm is applied. We use the ray paths computed in the 1-D velocity model. For any point of a ray, eight nodes of the parametrization grid are selected, so that they form a parallelogram, which contains the current point. Velocity inside the parallelogram is interpolated bilinearly. The elements of the matrix are computed as:

$$M_{ij}^{Vgp(s)} = -\frac{1}{\Delta V_j^{p(s)}} \int_{\gamma_i} \frac{\Delta U_j(s)}{V_0^2(s)} ds, \tag{13}$$

where i is the number of the ray (line of the matrix); j is the number of the parameter to be inverted (column of the matrix); γ_i is the ray path; $\Delta V_j^{p(s)}$ is the unit velocity variation at the jth node; $\Delta U_j\,(s)$ is the velocity variation at the current point of the ray due to velocity variation at the jth node; $V_0^2\,(s)$ is the reference velocity at the current point.

The elements M_{ij}^{dh} responsible for the Moho depth variation are computed as :

$$M_{ij}^{dh} = dh_{ij} \left[\sqrt{\sigma_1^2 - p^2} - \sqrt{\sigma_2^2 - p^2} \right], \tag{14}$$

if the source is located under the Moho, and

$$M_{ij}^{dh} = \left(dh_{ij}^1 + dh_{ij}^2\right) \sqrt{\sigma_1^2 - \sigma_2^2}, \tag{15}$$

for *Pn* and *Sn* rays,
where dh_{ij} denotes the variation of the Moho depth at one or two entry–exit points of the ith ray due to unit value of the Moho variation at the jth node.

The elements M_{ij}^{srce} responsible for the source corrections include four terms. The first three elements of spatial displacement of a source are equal to the elements of the slowness vector; the fourth element responsible for correction of the origin time is equal to one. The station correction elements M^{Stp} and M^{Sts} are also equal to one.

An additional block of the matrix allows regularization of smoothness of the obtained 2-D and 3-D fields. Each line of this block contains only two non-zero elements, which correspond to parameters in neighbouring nodes. The part of the data vector corresponding to this block is assigned as zero.

As a result of the matrix construction, we have 11 controlling coefficients responsible for the unknown parameters. W1 and W2 regulate 3-D *P* and *S* velocity anomalies. W3 affects the variations of the Moho depth. W4 and W5 control the *P* and *S* station corrections. W6, W7 and W8 are responsible for horizontal and vertical shifts of sources and for the origin time, W9, W10 and W11 regulate smoothing of the *P* and *S* velocity fields and 2-D distribution of the Moho depth. The greater the values of these last three coefficients, the smoother the solution that is obtained. Determination of all the coefficients in the matrix is a delicate problem. We found in the literature (e.g. Pavlis & Booker 1980) some attempts to formalize the process using analytical schemes. However, in our case, determination of weights for principally different sorts of parameters (e.g. velocity in km s^{-1}, time corrections, in seconds, and source shift, in km) with the use of these schemes was not successful. Indeed, there are too many factors that can influence these coefficients, such as quantity of data, number of different sorts of parameters, level of noise, etc. The problem of weighting and regularization definition is very serious in any tomographic study. Though some semblance of formalism has appeared in some studies (like the relationship between the rms and the amplitude of the recovered model), the

inversion parameters are always tuned by the authors to achieve the most reasonable pictures (even if it is not indicated in the text). In this study, to define the general level of the parameter values, we use the result of recovery tests (see Sections 5.3–5.5) in which the data are computed through some synthetic anomalies and spoiled by noise having a similar distribution as in the real data. However, we should confess honestly that the final tuning of the inversion parameters is performed manually to get the expected amplitudes of the parameters sought.

This matrix was inverted with the LSQR method (Paige & Saunders 1982; van der Sluis & van der Vorst 1987). The number of LSQR cycles necessary to provide a satisfactory convergence was 50.

After inversion, all the rays are traced from the newly updated sources. The traveltimes are computed taking into account source and station corrections, velocity anomalies and Moho depth variation updated after the previous inversion step. As a result, a new matrix and new residuals are computed, and the inversion is performed again. The iterative algorithm is repeated until the convergence is sufficient. This was achieved after five iteration steps.

4 RESULTS OF DATA INVERSION

In this section we show the results of real data inversion using starting Model 1 with the parameters shown in Table 1. We have tried several different variants of the reference models and various values of the inversion parameters. Some of them are compared in the Verification section. The general conclusion from many tests, some of which will be described later, is that the obtained anomalies are rather robust and weakly affected by changing the parameters and starting models. The velocity anomalies and Moho depth maps are obtained as the summary of four results computed in differently orientated grids after five iterations. For the main results we used a rather conservative rule for the grid construction: most of the parametrization nodes are located in the areas with the ray density five times higher than the average value. This means that for this model we get the solution only in places where the amount of input information is fairly high. Velocity anomalies and the Moho depth values are shown only if a distance to the nearest parametrization node is less than 15 km.

4.1 Source locations

In Fig. 8 we present the initial and final locations of the earthquakes in the whole study area and a zoom of the Dead Sea region. After location, the earthquakes are concentrated in a slightly narrower belt (∼20 km width) around the main DST fault. Between the Dead Sea and Sea of Galilee on the western flank, we observe an alignment of events that can be traced in a NNW direction for more than 100 km. This feature can be attributed to a series of faults between the Dead Sea and Mediterranean such as the Carmel fault system (e.g. Ben-Avraham & Ginzburg 1990).

Most events along the DST region occur in the crust in agreement with previous studies (e.g. Alderson *et al.* 2003). The few events obtained under the Moho beneath the Dead Sea can be considered rather as an exception than a regular feature, and taking into account the accuracy of location we cannot be sure that they indeed occur in the mantle and not in the lower crust. In general, around the DST the maximum number of events takes place in the depth interval of 15–20 km. This is consistent with estimates of crustal strength, which presume that maximum stresses are at a depth of about 20 km (Alderson *et al.* 2003). On the other hand, we can clearly distinguish

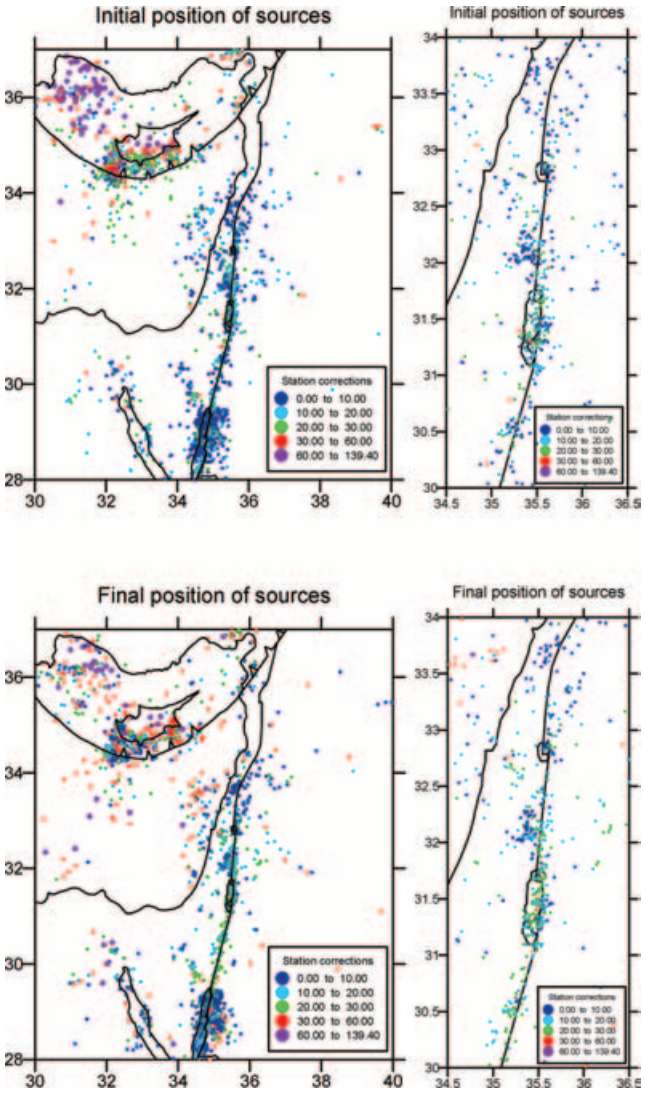

Figure 8. Initial and final, after full inversion procedure, position of sources. Right column is enlargement of the area around the DST. Depth of events is indicated with different colours according to the scale.

the depth distribution of the seismicity within and outside the Arava valley. Along the fracture zone of the DST, the earthquakes are mostly located in the lower crust, while outside the Arava valley, the events are shallower.

The reliability of depth determination for the events in the Levant basin is rather low. The depths of more than 30 km determined for many events under the Mediterranean are apparently not trustworthy. First of all, the azimuthal distribution of stations for these sources is poor. In addition, *Pn* and *Sn* rays that are dominantly recorded from these events, do not give good constraints on the depth of the events. Finally, in this area there are strong contrasts in Moho depth, and the model approximations might be too rough to give reliable depth determinations with the data available. In the Cyprus region, the events mark the Benioff zone and are observed down to a depth of 120 km.

4.2 Moho depth

Fig. 9 shows the map of the Moho depth obtained in Model 1, which uses a starting model with variable Moho depth of 1° × 1°

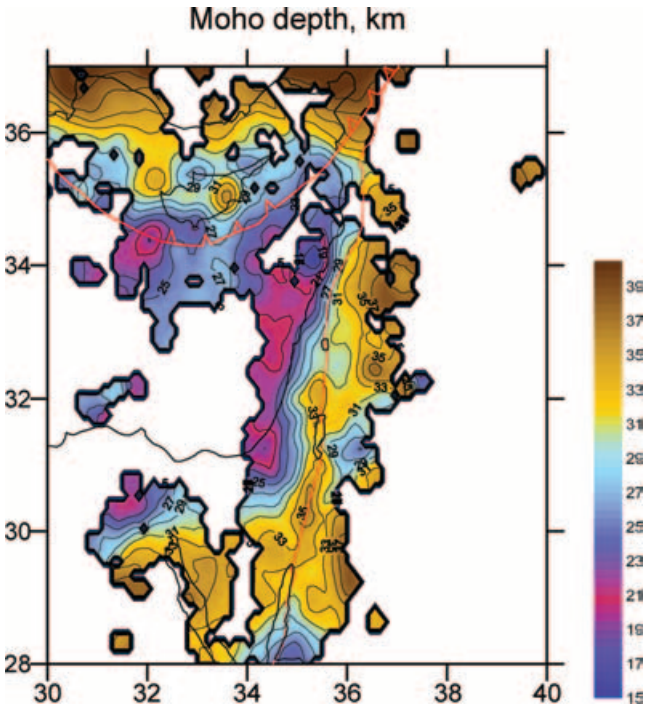

Figure 9. Map of the Moho depth derived from the real data inversion for Model 1 (main result). This result is obtained simultaneously with the velocity model shown in Fig. 10.

resolution (Laske, private communication, 2004). The resulting map reveals some large and small scale features, which have obvious relations with the existing geological units. In particular, it shows clear differentiation of continental and oceanic crust. In the Levant basin, the crust thins to 19 km, while in the continental parts the Moho depth varies between 27 and 37 km. The contrast between the continental and oceanic crust in the resulting model is much sharper than in the starting model (Fig. 3).

An important feature of the resulting model is a local crustal thickening along the DST between the Dead Sea and Red Sea, which reaches 33–35 km in some points. To the east of the Dead Sea there is an area of locally thinned crust in which the Moho depth reaches 27–29 km. All the synthetic tests as well as all other verification tests show that the resolution in this area is rather high and these features are reconstructed reliably (see Sections 5.1–5.4, 5.6 and 5.7). The implications of this result for the problem of the origin of the DST is discussed in Section 6.1.

A part of the study area coincides with the region of the DESERT project activity (DESERT Group 2004), where complex geophysical investigations were carried out. The domain of relatively thick crust on the eastern flank of the DST at the latitude of 30° seems to be consistent with the Moho topography inferred from gravity modelling (Götze *et al.*, private communication, 2005) and the receiver function study (Mohsen *et al.* 2005). The increase of Moho depth from 26 km at the Mediterranean coast to 39 km under the Jordanian highlands obtained in the wide-angle profile (DESERT Group 2004) is generally consistent with the results shown here (25 km and 36 km correspondingly). The discrepancy observed at the eastern edge of the profile can be explained by lower resolution in both studies in this boundary area.

Another striking feature of the Moho model is a relative crustal thickening of up to 33 km in Cyprus and 27 km under the Eratosthenes Seamount. This fact, together with observed low velocities in the lower crust and underneath the Moho, supports the interpretation that the crust in these blocks has a continental nature. This is consistent with a number of observations suggesting continental-type crust in this region (e.g. Garfunkel 1998; Ben-Avraham *et al.* 2002).

4.3 Velocity anomalies

The results of inversion for *P* and *S* velocity anomalies in the crust are presented in Fig. 10. The resolution in different parts of the area can be estimated from the results of synthetic tests shown in Fig. 11. In general, a rather good correlation of *P* and *S* anomalies is observed. In the uppermost section, at 5 km depth, a strong narrow low-velocity anomaly is observed along the Arava fault. The width of this anomaly in our images is 20–40 km, though in reality it could be narrower, because 15–20 km is the lower limit of resolution of our model. This anomaly is obviously a reflection of a sedimentary basin in the Arava valley, which is one of the thickest in the world. Another negative anomaly is observed in the NW direction from the northern edge of the Dead Sea basin. This area coincides with the zone of the Cermal fault system. The velocity decrease here is apparently due to fracturing of rocks. In the deeper sections the Arava fault is still traced in both *P* and *S* velocities, though the *S* image is less clear, probably due to a lack of resolution. In the Section 5.4 we will show a synthetic test with a sedimentary layer, which demonstrates the absence of vertical smearing of the uppermost anomalies downwards. This means that negative anomalies at the depth of 20 and 30 km cannot be related to the sediments observed in the uppermost part. These low-velocity patterns are probably due to the rock fracturing in the lower crust in the area of the DST. This is consistent with the distribution of seismicity under the Arava valley, which occurs mostly in the middle and lower crust (see Fig. 8).

The maps of *P* and *S* velocities in the uppermost mantle constructed on the basis of traveltimes of *Pn* and *Sn* rays are represented in the depth sections of 33 and 60 km. The boundary velocities, both *P* and *S*, clearly differentiate the continental and oceanic crust. Generally higher velocities are observed under the Levant basin. Low velocities occur in Asia Minor, Sinai Peninsula, Cyprus and the Eratosthenes Seamount, the areas where continental crust exists. Although our inversion reveals clear patterns in the mantle velocities, there are at least two points that force us to consider these results with some caution. First, there is a strong variation of thickness of the crust in the region, and although we invert for such variations, the remaining errors in crustal thickness may significantly affect results of the inversion for the velocities in the lower crust and sub-Moho mantle. We note that there is some apparent correlation between the Moho map (Fig. 9) and sub-Moho velocities (Fig. 10), suggesting that some trade-off may indeed exist between these parameters. Second, our model does not allow for seismic anisotropy, which in fact can strongly affect *Pn* and *Sn* velocities (Bamford 1973; Fuchs 1983; Enderle *et al.* 1996). Note also that strong seismic anisotropy was reported in the area of interest (Rümpker *et al.* 2003). For more discussion on possible interpretation of seismic velocities see Section 6.1.

5 VERIFICATION

To give more confidence to the presented results we have performed several tests. It is known that tomography natural sources is a poorly posed problem and the final results always depend on the initial model and parameters defined by a researcher. To understand how strong the influence of the starting model on the result is, after

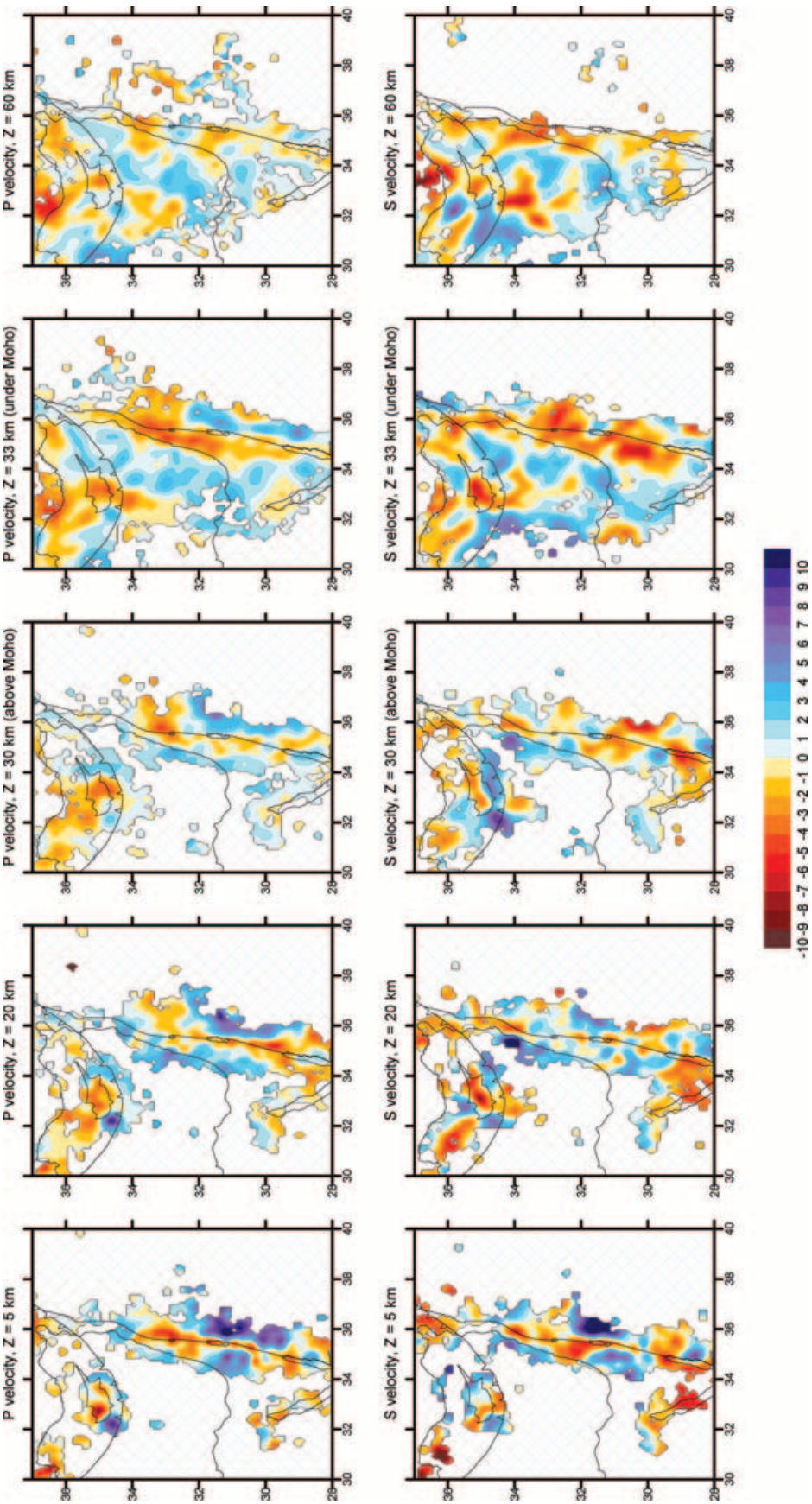

Figure 10. *P* and *S* velocity anomalies after five iterations of simultaneous inversion of real data (Model 1, main results).

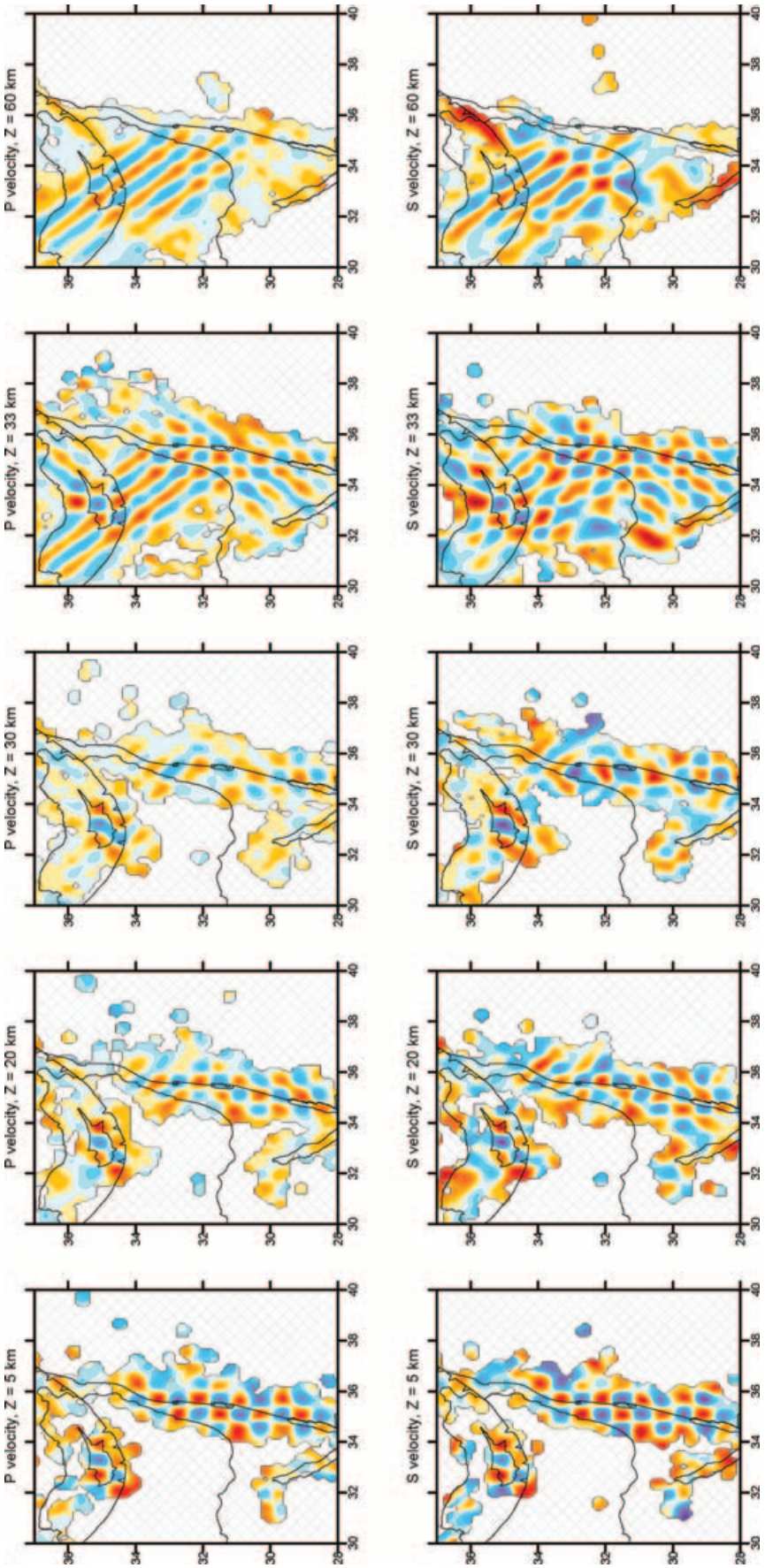

Figure 11. Synthetic test with chess-board anomalies. Velocity anomalies are defined as alternating positive and negative blocks of 0.6° size. Result of full tomographic inversion is shown in five horizontal sections. Upper row shows the resolution of *P* model, lower row corresponds to *S* model. The colour scale is the same as in Fig. 10.

obtaining the main results, we have performed two further inversions using different starting models: with a flat starting Moho (Section 5.1) and with a different velocity distribution in the crust (Section 5.2). The robustness of the results with respect to the noise in the real data is evaluated using independent inversions of two subsets of the data (test with odd and even events, Section 5.3). The resolution of the model is checked in a series of synthetic tests (Sections 5.4–5.6).

5.1 Model with a flat starting Moho

The full inversion procedure has been performed for the starting model with a 'flat' Moho fixed at the depth of 30 km (Model 2, Table 1), in contrast to the variable Moho model used in the main model. The velocity model and all other inversion parameters were the same as those used in the main model inversion. The results for the *P* and *S* velocity anomalies at two depths and the obtained Moho depth are shown in Fig. 12, upper row. The velocity anomalies in this case are practically identical to those obtained in the main model (Fig. 10). However, the difference between the Moho depth maps in these two cases is quite important, which is natural due to the non-uniqueness of the coupled tomographic problem. At the same time the most important features are observed in both maps: clear distinguishing of the oceanic and continental crusts along the east Mediterranean coast, elongated zone of thick crust along the DST, local thinning of the crust to the east of the Dead Sea Basin, thick crust under Cyprus, etc. Some differences in the marginal areas, such as crust that is thinner than it should be in the eastern and northern sides of the study region, are apparently due to lack of data.

5.2 Model with another starting velocity model and 'liberal' parametrization algorithm

Fig. 12, lower row, shows another inversion result derived using another starting velocity model (Model 3). The values of *P* and *S* velocities are shown in Table 1. In this model we have significantly changed the velocity gradients in the crust as well as the ratio Vp/Vs. Obviously these differences cause shifts of the relocated sources and change the ray paths. Nevertheless we have obtained a paradoxical result, in that neither velocity anomalies nor the Moho depth are strongly affected by changes in the reference velocity model. In other words, the data set used in this study does not provide any constraint on the reference velocity model and, therefore, there is no sense to show the absolute velocities in the final results. Even if we make a mistake in the definition of the reference velocity model, the resulting images of the velocity anomalies would remain unchanged with respect to those derived from a true model.

In this test we also explore the effect of differences in the construction of parametrization grids. As we have already mentioned, the algorithm allows tuning of the 'conservatism' of the model. In the main result we used a 'conservative' grid, in which most of the nodes are installed only if the density of information is five times higher than the average level. In this test, the method of parametrization is more 'liberal', in that we allow the nodes to be installed in those areas where the density of information is just higher than the average level. The 'liberal' model covers a larger area. However, as we can judge from synthetic tests, the resolution in the marginal parts of the 'liberal' model is significantly lower. In the overlapping area both models give similar results.

5.3 Test with odd and even events

To evaluate the contribution of the random noise in the data we perform independent inversions of two data subsets. Subdivision is performed in a random way, for example, events with odd and even numbers. In this case, we used the same inversion procedure as in the main data processing. The results are shown in Fig. 13. We observe a rather high coherency of velocity anomalies in the crust and almost perfect correlation for the Moho depth that gives high confidence to these results. At the same time, in the upper mantle the resemblance of the velocity images is much poorer, which indicates a high influence of noise upon the results at these depths. However, the positions of the main significant patterns in the upper mantle, such as a contrast between the oceanic and continental parts and a low-velocity anomaly beneath the Eratosthenes Seamount, are reconstructed reliably in both models.

5.4 Chess-board test

To evaluate the sensitivity of the model in different parts of the study area, we perform a chess-board test. The initial synthetic model is defined in the whole area as periodical chess-board anomalies of 0.6° size and 5 per cent amplitude both for *P* and *S* models. Similar patterns are defined for the Moho interface to check the resolution of the Moho depth reconstruction. In this case the size of anomalies was 0.7° and the amplitude was ±5 km. The time residuals for the synthetic test are computed along the rays traced in the 1-D reference model with the positions of sources and receivers corresponding to the real observation system. The delay related to the velocity anomaly of a body is integrated along a ray γ as:

$$dt^{\mathrm{vel}} = -\int_{\gamma} \frac{0.01 \;\; dV(\text{per cent})}{V_0} \; ds. \tag{16}$$

Delays related to the crustal thickness variation, dt^{cr} are computed at the entry and exit points with the use of the formulae for the crustal corrections [formulae (1) and (2)]. Both these residuals are included in the synthetic data simultaneously. The 'observed' traveltimes for the synthetic test are computed as a sum of the traveltime in the reference model, synthetic delays and random noise:

$$T^{\mathrm{obs}} = T^{\mathrm{ref}} + dt^{\mathrm{vel}} + dt^{cr} + \varepsilon, \tag{17}$$

where ε is the random noise with a magnitude estimated from the real data dispersion (0.3 s on average). These times are the input for the whole inversion procedure, including the step of absolute source location. The values of the inversion parameters for the synthetic test are the same as those used for the real data inversion.

The results of the reconstruction of the *P* and *S* velocity models after five iteration steps for four differently orientated grids are shown in Fig. 11. In the crust, the best resolution is achieved along the DST fault from Aqaba to the Sea of Galilee. Rather good resolution is also observed in the area of Cyprus. In the upper mantle rather high resolution is observed under the Levant basin, though the anomalies are smeared in the NW direction. In Fig. 14 the result of the reconstruction of the Moho depth anomalies is presented. As in the case of the velocity anomalies, the best resolution is achieved in the areas of the DST and Cyprus where rather fine details can be resolved.

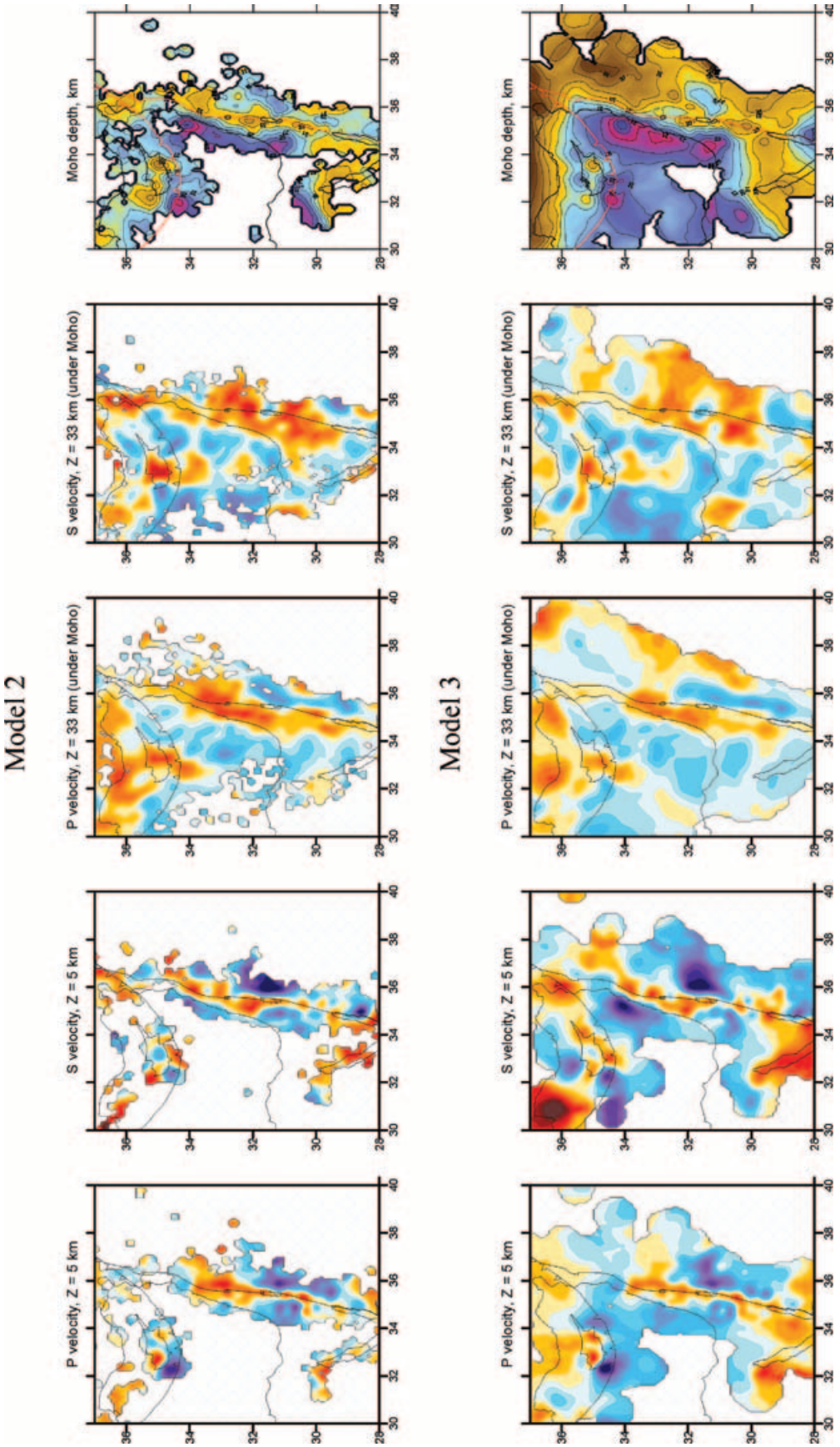

Figure 12. Inversion with different starting models and parametrization parameters. Upper row corresponds to Model 2, which is similar to Model 1 (main result, Figs 9 and 10), but with a flat Moho at 30 km depth. Lower row is the result for the Model 3 with the same Moho model, as in Model 1, but with a different velocity model (see text). Examples of *P* and *S* velocity anomalies in two depth sections (5 and 33 km) and Moho depth maps are shown. The colour scale is the same as in Figs 9 and 10.

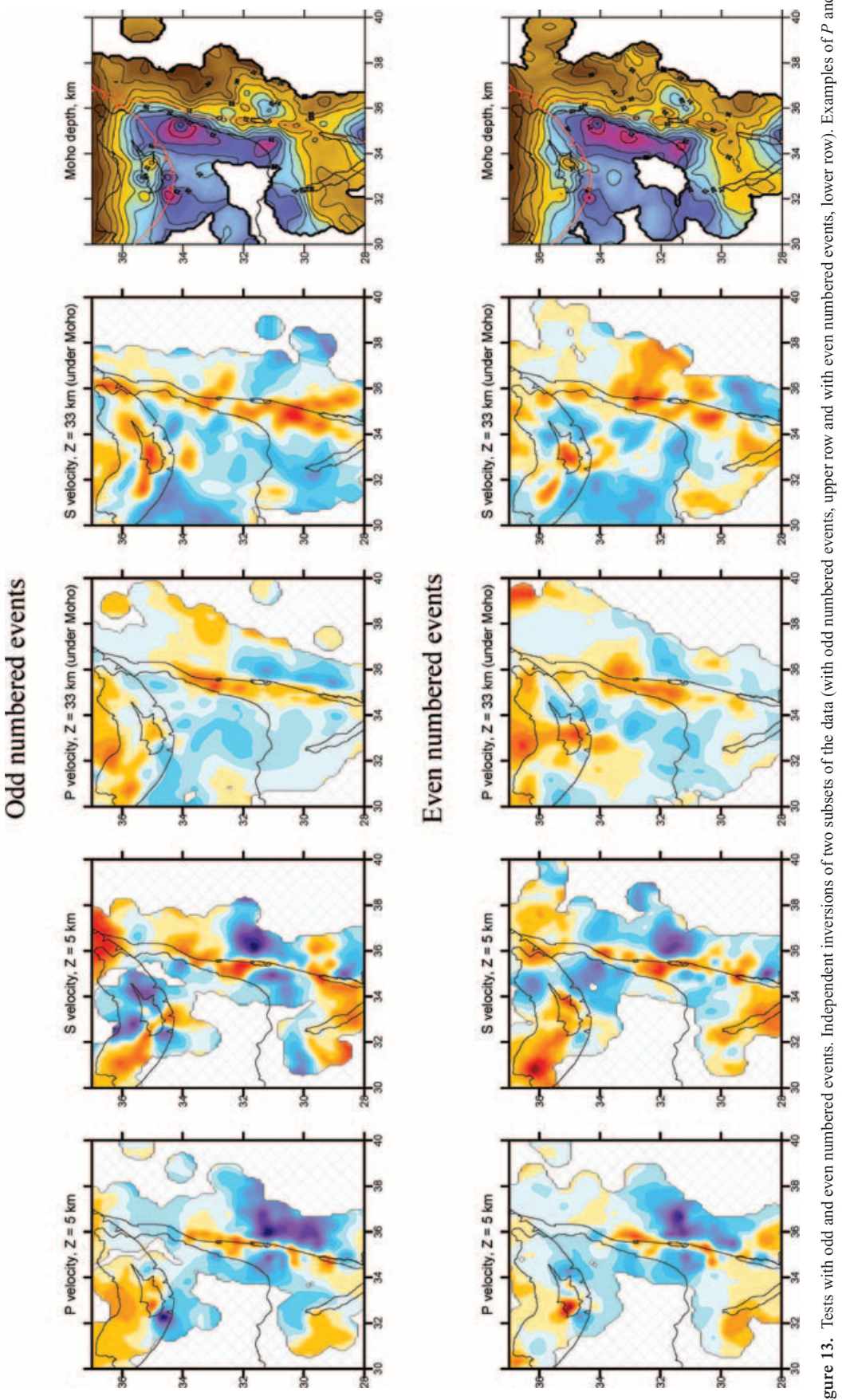

Figure 13. Tests with odd and even numbered events. Independent inversions of two subsets of the data (with odd numbered events, upper row and with even numbered events, lower row). Examples of *P* and *S* velocity anomalies in two depth sections (5 and 33 km) and Moho depth maps are shown. The colour scale is the same as in Figs 9 and 10.

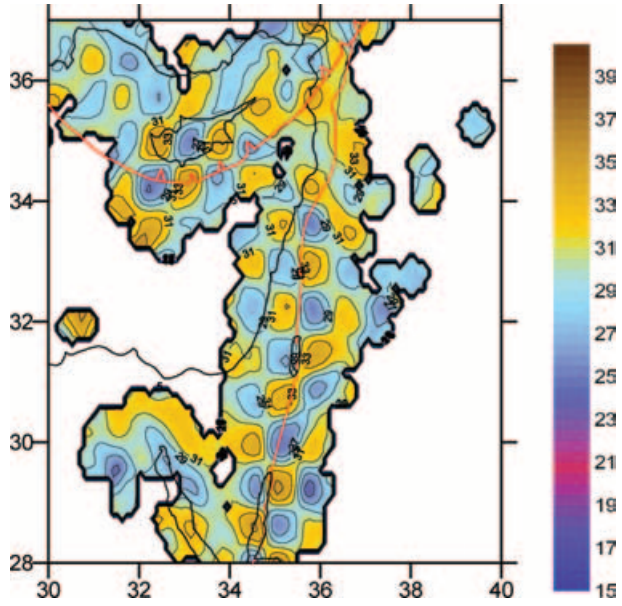

Figure 14. Result of reconstruction of the chess-board anomalies of the Moho depth with a size of 0.7°. This result is obtained simultaneously with the velocity model shown in Fig. 11. The colour scale is the same as in Fig. 9.

5.5 Can the sediments affect the images of deep structures?

To answer the question about influence of the near-surface anomalies upon the deeper velocities and Moho depth reconstruction, we have performed another test with a synthetic anomaly (−10 per cent of *dVp* and *dVs*) located along the DST in the depth range from 0 to 5 km. This anomaly is a model of a thick sediment layer, which is presumed in the Arava valley. The procedure of synthetic time calculation and inversion was the same as for the chess-board test described above. The results of inversion are shown in Fig. 15. This test shows rather good vertical resolution, which does not allow the anomaly to smear downwards. In the sections at 5 km depth the contours of the 'sediments' are reconstructed rather clearly. In the sections at 20 km depth we observe a minor replica of the anomaly at 5 km depth of opposite sign. In deeper sections and in the Moho depth map we do not see any influence of the uppermost anomalies.

In this test we also modelled the capacity of the algorithm to resolve a low-velocity continental crust in Cyprus. An anomaly of −5 per cent amplitude was defined within the island down to 20 km depth. The reconstruction of this anomaly shown in Fig. 15 is satisfactory, especially in the shallower layer.

5.6 Test with fancy figures

To check the capacity of the algorithm to separate rather complicated anomalies having different shapes in the crust, uppermost mantle and in the Moho topography we have performed a test with fancy figures. The shapes of the initial anomalies (dancing figures taken from the painting by I.Koulakov 'Love Parade') are shown in Fig. 16. In the crust, the velocity anomalies are defined in the depth range between 0 and 30 km, whereas in the upper mantle, the anomalies are between 31 and 100 km depth. The test with such 'non-formal' anomalies shows better the realistic resolution compared to a chess-board test. The periodicity predefined by the chess-board anomalies is always manifested in the results of the inversion and, as a result, the resolution plots can be nicer than they should be in reality. In

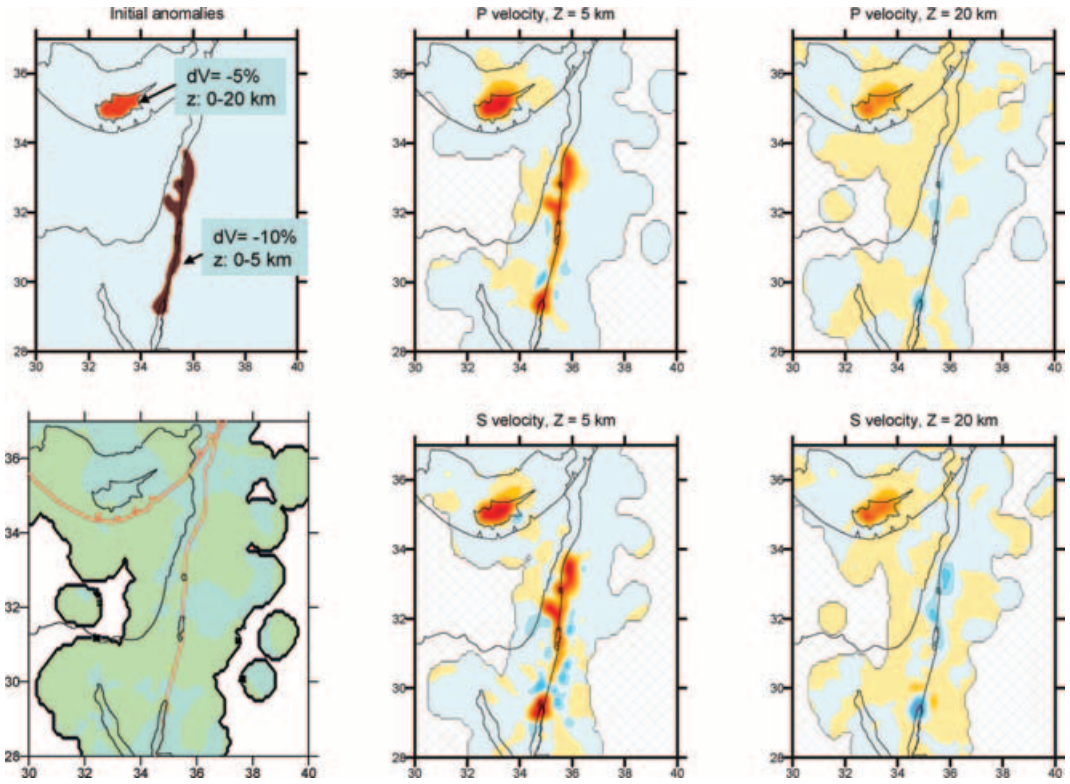

Figure 15. Synthetic test with 'a sediment layer' in the Arava valley and 'Continental crust' in Cyprus. Upper left map shows the shape of the initial anomalies with indication of their parameters. Lower left plot is reconstruction of the Moho depth, which demonstrates insignificant variations. Central and right columns show results of reconstruction for *P* (upper row) and *S* (lower row) anomalies at 5 and 20 km depth.

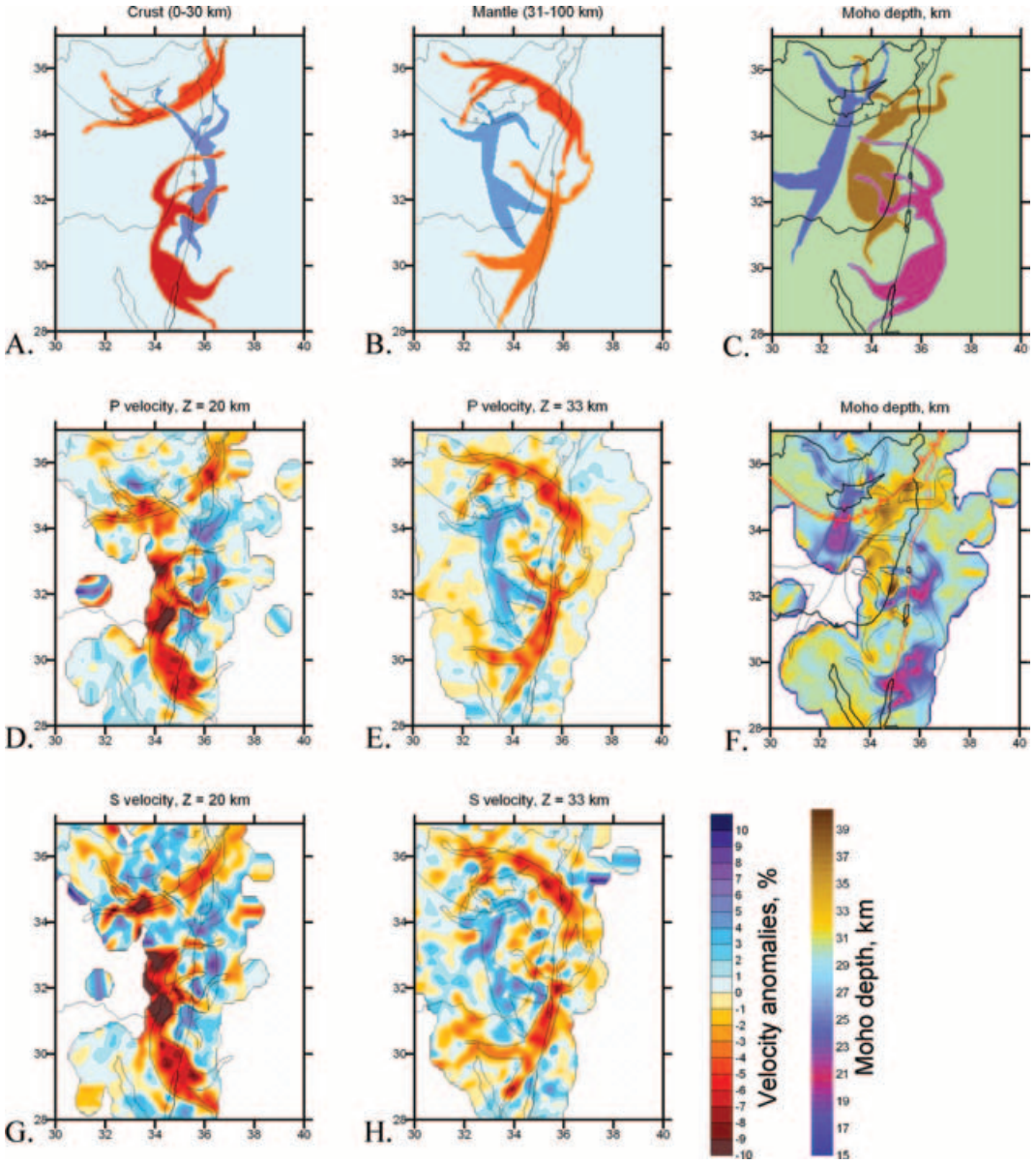

Figure 16. Synthetic test with fancy figures. Upper row shows initial shape of anomalies: (a) *P* and *S* velocities in the crust (0–30 km), (b) *P* and *S* velocities in the mantle (33–100 km). (c) Initial shape of the Moho topography. (d) Results of reconstruction of the synthetic anomaly in *P* velocity in the crust (horizontal section at 20 km depth). (e) Same as (d), but for *P* velocities in the mantle (33 km depth), (f) Reconstructed Moho depth, (g) Same as (d), but for S velocities in the crust (20 km depth), (h) Same as (d), but for *S* velocities in the mantle (33 km depth).

addition, a complex shape of figures allows one to obtain an idea about the reconstruction of different scale objects (fancy figures as a whole or their details). After realization of this test (Fig. 16D–H), we can see fairly good reconstructed fancy figures in the areas where the resolution is sufficient. It is important that the velocity anomalies in the crust and the uppermost mantle and anomalies of the Moho depth do not interfere with each other, as could be expected in simultaneous inversion.

5.7 Trade-off between Moho topography and velocity structure

The key result of this paper is the map of the Moho topography. As we have seen above, the resolution of the map in most interesting domains such as the DST is fairly good. However, there may be a trade-off between seismic velocity structure and Moho topography. To test this possibility we have run an inversion in which only very minor velocity variations in the crust and the mantle (less than 1 per cent) were allowed. The encouraging result of this test is that the resulting Moho topography map (Fig. 17) does not differ much from the map calculated for the model where much larger variations of seismic velocities were allowed (Fig. 9). This means that the main features of the Moho topography derived in our inversion are robust and do not depend on the uncertainties of the seismic velocity structure.

6 DISCUSSION AND CONCLUSIONS

6.1 Implications for the structure and origin of the DST

One of the key questions concerning the Cenozoic tectonic evolution of the Middle East is the question of what controls the location of the

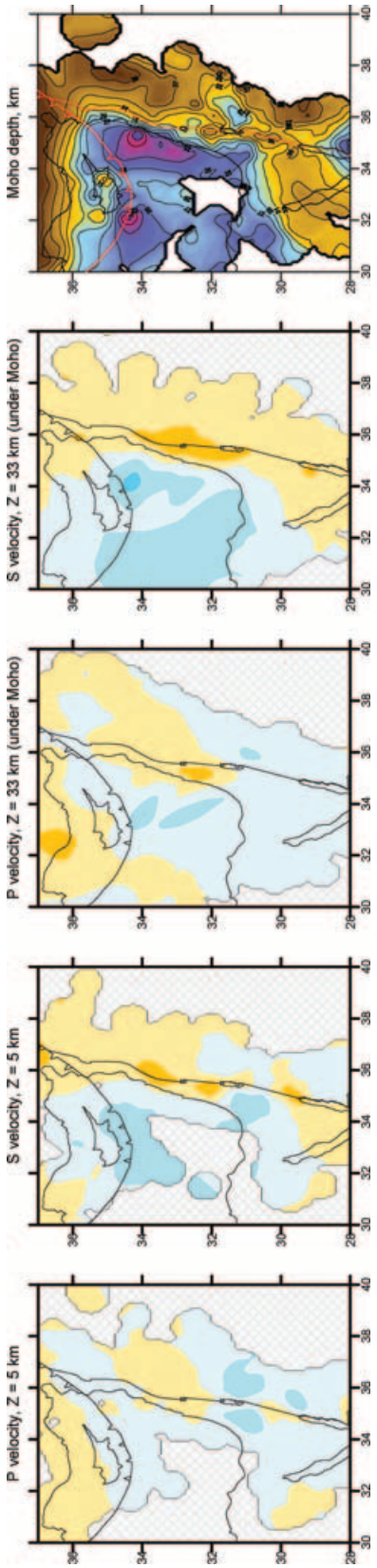

Figure 17. Test for investigation of possible trade-off between velocity models and Moho depth. In this test we use the same inversion procedure and tuning parameters as in the main model (Figs 9 and 10), except for the weights of *P* and *S* velocity parameters, which were defined to be five times smaller. The result of the inversion shows very weak velocity anomalies and an unchanged image of the Moho depth, which indicates the negligible trade-off between these parameters.

DST. Steckler and Ten-Brink (1986) suggested that the DST north of the Dead Sea follows the zone of minimum lithospheric strength at the Mediterranean margin, while to the south of the Dead Sea, where this margin becomes too oblique to the plate motion direction, the DST runs parallel to the plate velocity. In this hypothesis the lithospheric heterogeneity south of the Dead Sea did not play a role in the localization of the DST. Sobolev *et al.* (2005) studied the evolution of the deformation at the DST using a numerical thermomechanical modelling technique. They showed that the strike-slip deformation does localize in the zones of minimum lithospheric strength, which may correspond either to a regional thickening of the crust or to a regional thinning of the lithosphere or to the margin of a thick lithospheric root at a passive continental margin. They suggested that south of the Dead Sea, the location of the DST may have been also controlled by the regional strength minimum.

The map of the Moho topography obtained in this study (Fig. 9) allows a new consideration of the question of what controls the location of the DST. For a constant thickness of the lithosphere, lithospheric strength is approximately inversely proportional to the thickness of the crust (Sobolev *et al.* 2005). In this simplified case, the Moho map (Fig. 9) may be considered as a proxy for a map of lithospheric strength. From this map we see that north of 32°N the DST trace goes around the zone of high strength represented by the thin crust of the Mediterranean. This feature basically agrees with the suggestion of Steckler & ten Brink (1986). However, between 32°N and 29.5°N, where according to Steckler & ten Brink (1986) the direction of the DST is just parallel to the plate velocity, the DST in fact traces the regional strength minimum (thicker crust). From this we conclude that between the Dead Sea and the Red Sea (Gulf of Aqaba) the location of the DST might have been controlled by the inherited crustal structure resulting in a regional minimum of the lithospheric strength in agreement with the suggestion based on the numerical model of Sobolev *et al.* (2005).

Another important question related to the DST is how important was the rifting (fault perpendicular extension) deformation component at the DST (Garfunkel 1981). The Moho topography map (Fig. 9) does not show any evidence of localized crustal thinning along the DST, which would be expected if a rifting deformation component was significant. Moreover the dominant tendency is exactly the opposite, with thicker crust at the DST. This observation provides further evidence for the relatively small importance of the rifting deformation component at the DST in agreement with geological observations (Garfunkel 1981), recent seismic observations (DESERT Group 2004) and thermomechanical modelling (Sobolev *et al.* 2005). Interestingly, no crustal thinning is imaged also beneath the Dead Sea. This indicates that if any significant Moho uplift exists here it must be very narrow, and less than the distance of 20 km between the model grid points in this region, such that our tomographic study cannot resolve it.

Although the interpretation of the seismic velocity images (Fig. 10) may be controversial (e.g. due to the possible effect of unconsidered seismic anisotropy), what is obvious from the *P*-wave structure (Fig. 10, upper row) is that the DST itself is visible throughout the entire crust and in the uppermost mantle. As is demonstrated by several resolution tests (see Section 5) this feature is quite robust. From this we conclude that the DST penetrates through the entire crust in agreement with the recent controlled source seismic study (DESERT Group 2004) and modelling study (Sobolev *et al.* 2005).

As we mentioned above, there is a tendency towards a deepening of the seismicity close to the DST (see Fig. 8). We suggest a simple explanation of this phenomenon in relation to the large strike-slip strain rate characteristic of this plate boundary. The downdip limit

of seismicity corresponds to the brittle–ductile transition, the depth of which is defined by the point where the stresses required to drive deformation in the brittle and ductile deformation regimes are equal. Now, yield stress in the brittle deformation regime (Mohr Coulomb stress) increases with depth but does not depend on the strain rate, while stress in the ductile deformation regime increases with the strain rate. Therefore, if the strain rate increases, the new point where both brittle and ductile stresses are equal is shifted to higher stress, that is, moves deeper. From this we conclude that deepening of the depth of seismicity close to the DST is consistent with the expected consequence of the high strain-rate strike-slip deformation in this region.

6.2 Conclusions

In this study we pay special attention to the problem of verification of the results, which is very important in the case of tomography using natural sources with unknown locations. In spite of fairly high noise levels in the ISC data and low values of variance reduction (30 per cent only), the data inversion provides rather robust images supported by a number of tests, such as reconstruction using different starting models and tests with odd and even numbered events. Moreover, the high correlation between *P* and *S* velocity anomalies and clear geodynamical interpretation of the obtained images also corroborate the reliability of the results.

In the main results of data inversion we can single out the following essential features:

(i) An elongated anomaly of thickened crust under the DST between the Dead Sea and Red Sea likely marks the position of the regional minimum of the lithospheric strength controlling the location of the DST in this region.

(ii) The DST is visible in the seismic images of the crust and uppermost mantle, suggesting that it crosses the entire crust. In the crust along the Arava valley, low-velocity *P* and *S* anomalies are imaged, which can be interpreted as sediments in the shallowest section, and as a zone of fractured rocks around the fault in the deeper sections;

(iii) In the upper mantle, the velocities clearly mark two types of the crust: high-velocity oceanic (Levant basin in Eastern Mediterranean) and low-velocity continental crust (Asia Minor, Zagros and Cyprus with Eratosthenes Seamount).

The main results of this study are the new information on the crustal structure, which can be used in different geophysical and geological domains. The new velocity model and crustal thickness map can be employed for improved determination of source parameters in the eastern Mediterranean and Asia Minor. In addition, the model of the Moho depth can be integrated into gravity studies for subtraction of crustal effects. The residual gravity anomaly will allow investigation of mantle anomalies. Moreover, this model can be introduced into teleseismic inversion (e.g. Hofstetter *et al.* 2000), which would allow more reliable imaging of the upper mantle beneath the Middle East. The complex shape of the Moho should be taken into account for migration of active 2-D seismic profiles because the reflected rays can be significantly 3-D. The map of the Moho depth presented here can be used for planning of future active deep seismic experiments.

Further improvement of the model is possible. First of all, the model can be updated with the new information accumulated after the year 2001, the last year of the catalogue data used to date. In addition, the data of local networks, which are not included into the ISC catalogue would also help to improve the resolution of the model. An important feature of this region is seismic anisotropy both in the crust and upper mantle, as demonstrated by the SKS splitting study (Rümpker *et al.* 2003). As some studies in the San Andreas Fault area show (Paulssen 2004), the difference in traveltimes along and across the transform fault can be fairly large. This indicates that seismic anisotropy associated with the large transform faults can play a major role in determining the seismic structure of the crust and mantle. Therefore, the next step is to develop the algorithm for anisotropic tomography and to apply it in the DST region.

ACKNOWLEDGMENTS

We are grateful to Alexei Petrunin for discussions about the geodynamical regime in the Dead Sea region. We thank Zvi Garfunkel for remarks, which were very useful for correction of the interpretation part. Our special thanks are addressed to Michael Weber, James Mechie, Ron Hackney and Rami Hofstetter for their unselfish help in revision of the manuscript. We are grateful to Claudia Piromallo and another anonymous reviewer for fruitful criticism. This study is partly supported by the DESERT project.

REFERENCES

Alderson, F., Ben-Avraham, Z., Hofstetter, A., Kissling, E. & Al-Yazjeen, T., 2003. Lower-crustal strength under the Dead Sea basin from local earthquake data and rheological modeling, *Earth planet. Sci. Lett.,* **214,** 129–142.

Al-Zoubi, A. & Ben-Avraham, Z., 2002. Structure of the Earth's crust in Jordan from potential field data, *Tectonophysics,* **346,** 45–59.

Bamford, D., 1973. Refraction data in western Germany—a time-term interpretation, *Z. Geophys.,* **39,** 907–927.

Bassin, C., Laske, G. & Masters, G., 2000. The Current Limits of Resolution for Surface Wave Tomography in North America, *EOS, Trans. Am. geophys. Un.,* **81,** F897.

Beloussov, V.V., Pavlenkova, N.I. & Egorkin, A.V., 1991. Deep Structure of the Territory of the USSR., Nauka, Moscow p. 224.

Ben-Avraham, Z. & Ginzburg, A., 1990. Displaced terranes and crustal evolution of the Levant and eastern Mediterranean, *Tectonics,* **9**(4), 613–622.

Ben-Avraham, Z., Ginzburg, A., Makris, J. & Eppelbaum, L., 2002. Crustal structure of the Levant Basin, eastern Mediterranean, *Tectonophysics,* **346,** 23–43.

Bijwaard, H., Spakman, W. & Engdahl, R., 1998. Closing the gap between regional and global travel time tomography, *J. geophys. Res.,* **103,** 30 055–30 078.

Blundell, D., Freeman, R. & Mueller, S., 1992. St., Editors, *A Continent Revealed: The European Geotraverse*, Cambridge Univ. Press, Cambridge p. 276.

DESERT Group, *et al.*, 2004. The crustal structure of the Dead Sea Transform, *Geophys. J. Int.,* **156**(3), 655.

El-Isa, Z., Mechie, J., Prodehl, C., Makris, J. & Rihm, R., 1987. A crustal structure study of Jordan derived from seismic refraction data, *Tectonophysics,* **138,** 235–253.

Enderle, U., Mechie, J., Sobolev, S. & Fuchs, K., 1996. Seismic anisotropy within the uppermost mantle of southern Germany, *Geophys. J. Int.,* **125,** 747–767.

Evans, J.R., Eberhart-Phillips, D. & Thurber, C.H., 1994. User's manual for SIMULPS12 for imaging Vp and Vp/Vs: a derivative of the Thurber tomographic inversion SIMUL3 for local earthquakes and explosions, *U.S. Geol. Surv. Open-File Report 94-431*, U.S. Government Printing Office.

Freund, R., Garfunkel, Z., Zak, I., Goldberg, M., Weissbord, T. & Derin, B., 1970. Th eshear along the Dead Sea rift. Phylos, *Trans. R. Soc. London, Ser. A,* **267,** 107–130.

Fuchs, K., 1983. Recently formed elastic anisotropy and petrological models for the continental subcrustal lithosphere in southern Germany, *Phys. Earth. planet. Inter.,* **31,** 93–118.

Garfunkel, Z., 1981. Internal structure of the Dead Sea leaky transform (rift) in relation to plate kinematics, *Tectonophysics,* **80,** 81–108.

Garfunkel, Z., 1998. Constrains on the origin and history of the Eastern Mediterranean basin, *Tectonophys.,* **298,** 5–35.

Ginzburg, A., Makris, J., Fuchs, K., Prodehl, C., Kaminski, W. & Amitai, U., 1979. A seismic study of the crust and upper mantle of the Jordan-Dead Sea Rift and their transition toward the Mediterranean Sea, *J. geophys. Res.,* **84,** 1569–1582.

Ginzburg, A. & Ben-Avraham, Z., 1992, Crustal structure and tectonic processes in the Levant and the eastern Mediterranean, *Isr. J. Earth Sci.,* **40,** 125–133.

Ginzburg, A. & Ben-Avraham, Z., 1997. A seismic refraction study of the north basin of the Dead Sea, Israel, *Geophys. Res. Lett.,* **24**(16), 2063–2066.

Hofstetter, A. & Bock, G., 2004. Shear-wave velocity structure of the Sinai subplate from receiver function analysis, *Geophys. J. Int.,* **158,** 67–84.

Hofstetter, A., Feldman, L. & Rotstein, Y., 1991. Crustal structure of Israel: constraints from teleseismic and grevity data. *Geophys. J. Int.,* **104,** 371–379.

Hofstetter, A., Dorbath, C., Rybakov, M. & Goldshmidt, V., 2000. Crustal and upper mantle structure across the Dead Sea rift and Israel from teleseismic P-wave tomography and gravity data, *Tectonophys.,* **327,** 37–59.

International Seismological Centre, 2001. Bulletin Disks 1–9 [CD-ROM], Internatl. Seis. Cent., Thatcham, UK.

Kennett, B.L.N., Engdahl, E.R. & Buland, R., 1995. Constraints on seismic velocities in the Earth from traveltimes, *Geophys. J. Int.,* **122,** 108–124.

Koulakov, I. Yu., 1998. 3D tomographic structure of the upper mantle beneath the central part of Eurasian continent, *Geophys. J. Int.,* **133**(2), 467–489.

Koulakov, I., Tychkov, S., Bushenkova, N. & Vasilevskiy, A., 2002. Structure and dynamics ovf the upper mantle beneath the Alpine-Himalayan orogenic belt, from teleseismic tomography, *Tectonophys,* **358,** 77–96.

Kovach, R., Andresen, G., Getlings, M. & El-Kaysi, K., 1990. Geophysical investigations in Jordan, *Tectonophys.,* **180,** 61–69.

Li, S. & Mooney, W.D., 1998, Crustal structure of China from deep seismic sounding profiles, *Tectonophysics,* **288,** Issues 1–4, **30**, 105–113.

Makris, J., Ben-Avraham, Z., Behle, A., Ginzburg, A., Giese, P., Steinmetz, L., Whitmarsch, R.B. & Eleftheriou, S., 1983. Seismic refraction profiles between Cyprus and Israel and their interpretation, *Geophys. J. R. astr. Soc.,* **75,** 575–591.

Martinez, M.D., Lana, X., Canas, J.A., Badal, J. & Pujades, L., 2000. Shear-wave tomography of the lithosphere-asthenosphere system beneath the Mediterranean area, *Phys. Earth planet. Int.,* **122,** 33–54.

Meissner, R., Wever, T. & Fluh, E.R., 1987. The Moho in Europe — implications for crustal development, *Annales-Geophysicae,-Series-B.,* **5B**(4), 357–364.

Mohsen, A., Hofstetter, R., Bock, G., Kind, R., Weber, M., Wylegalla, K., Rümpker, G. & DESERT Group, 2005. A receiver function study across the Dead Sea Transform, *Geophys. J. Int.,* **160,** 948–960.

Mooney, W.D., Laske, G. & Masters, G., 1998. Crust 5.1: a global crustal model at 5 × 5 degrees, *J. geophys. Res.,* **103,** 727–747.

Paige, C.C. & Saunders, M.A., 1982. LSQR: An algorithm for sparse linear equations and sparse least squares, *ACM trans. Math. Soft.,* **8**(1), 43–71.

Pasyanos, M.E. & William, R.W., 2002. Crust and upper mantle structure of North Africa, Europe and the Middle East from inversion of surface waves, *Geophys. J. Int.,* **149,** 463–481.

Paulssen, H., 2004. Crustal anisotropy in Southern California from local earthquake data, *Geophys. Res. Lett.,* **31,** L01601, doi:10.1029/2003GL018654.

Pavlis, G.L. & Booker, J.R., 1980. The mixed Discrete-Continuous inverse problem: application to the simultaneous Determination of earthquake hypocenters and velocity structure, *J. geophys. Res.,* **85,** 4801–4810.

Piromallo, C. & Morelli, A., 2003. *P* wave tomography of the mantle under the Alpine-Mediterranean area, *J. geophys. Res.,* **108**(B2), 2065, doi:10.1029/2002JB001757.

Rümpker, G., Ryberg, T., Bock, G. & Desert Seismology Group, 2003. Evidence for boundary-layer mantle flow beneath the Dead Sea Transform from seismic anisotropy, *Nature,* **425,** 497–501.

Rybakov, M., Goldshmidt, V., Fleischer, L. & Ben-Gai Y., 2000. 3-D gravity and magnetic interpretation for the Haifa Bay area (Israel), *J. appl. Geophys.,* **44,** Issue 4, 353–367.

Sandvol, E., Seber, D., Calvert, A. & Barazangi, M., 1998. Grid search modelling of receiver function: implications for crustal structure in the Middle East and North Africa. *J. geophys. Res.,* **103**(b11) 26 899–26 917.

Seber, D., Vallve, M., Sandvol, E., Steer, D. & Barazangi, M., 1997. Middle East tectonics: applications of geographic information systems (GIS), *GSA-Today,* **7/2,** 1–6.

Seber, D., Sandvol, E., Sandvol, C., Brindisi, C. & Barazangi, M., 2001. Crustal model for the Middle East and North Africa region: implications for the isostatic compensation mechanism, *Geophys. J. Int.,* **147,** 630–638.

Sobolev, S.V., Petrunin, A., Garfunkel, Z., Babeyko, A.Y. & DESERT Group, 2005. Thermo-mechanical model of the Dead Sea Transform, *Earth planet. Sci. Lett.,* **238,** 78–95.

Spakman, W., 1991. Delay-time tomography of the upper mantle below Europe, the Mediterranean and Asia Minor, *Geophys. J. Int.,* **107,** 309–332.

Steckler, M.S. & ten Brink, U.S., 1986. Lithospheric strength variations as a control on new plate boundaries; examples from the northern Red Sea region, *Earth planet. Sci. Lett.,* **79,** 120–132.

ten Brink, U., Ben Avraham, Z., Bell, R., Hassonneh, M., Coleman, D., Andreasen, G., Tibor, G. & Coakley, B., 1993. Structure of the Dead Sea pull-apart basin from gravity analysis, *J. geophys. Res.,* **98**(21), 877–894.

Thurber, C.H., 1993. Local earthquake tomography: velocities and VP/VS theory, in *Seismic Tomography: Theory and Practice*, eds Iyer, H.M. & Hirahara, K., Chapman and Hall, London, UK (GBR).

van der Sluis, A. & van der Vorst, H.A., 1987. Numerical solution of large, sparse linear algebraic systems arising from tomographic problems, in *Seismic tomography*, pp. 49–83, ed. Nolet, G., Reidel, Dortrech.

Waldhauser, F. & Ellsworth, W.L., 2000. A double-difference Earthquake location algorithm: method and application to the northern Hayward fault, California, *Bull. seism. Soc. Am.,* **90**(6), 1353–1368.

Ziegler, P.A., 1990, Geological Atlas of Western and Central Europe. *Shell Internat. Petrol. Mij. and Geol. Soc.*, *London*, *p. 239 and 56 encl.*